Corner singularities and shape of stretched elastic sheets

Julien Chopin
Instituto de Física, Universidade Federal da Bahia, Salvador-Bahia 40170-115, Brazil

Andreea Panaitescu and Arshad Kudrolli
Department of Physics, Clark University, Worcester, Massachusetts 01610, USA

(Received 27 July 2018; published 17 October 2018)

We investigate the deformation of a longitudinally stretched rectangular sheet which is clamped at two opposite boundaries and free otherwise with experiments, numerical analysis, and asymptotic analysis of the biharmonic elastic equation governing their planar equilibrium configurations. The displacement field of the sheet is measured by tracking embedded fluorescent tracers with a digital image correlation technique. The experiments and numerical finite-element analysis are found to be in overall good agreement except at the very corners where large deformations occur. We find that the deformed sheet can be broadly divided into a uniaxially stretched central region and two clamp-dominated side regions. A subregion characterized by a diverging stress can be identified at each of the four clamped-free corners within the clamp-dominated region. We postulate that the divergence at the corners is regularized by nonlinear elastic deformations occurring in this subregion at the very corners and provide a nontrivial scaling for its size. Within the intermediate corner-dominated subregion, measured displacements grow with distance r from the corners as r^{α}, with power $\alpha < 1$ consistent with the development of stress singularities at the intersection of the free and clamped edges.

DOI: 10.1103/PhysRevE.98.043003

I. INTRODUCTION

A stretched thin elastic sheet is a paradigm in understanding the shape and instabilities of highly deformable elastic solids [1–4]. Rectangular sheets stretched longitudinally, while clamped at two opposite edges, contract transversely at the free edges due to Poisson's effect. As is by now well known, wrinkles may occur for sufficiently thin sheets [3,5], but their exact nature remains a matter of debate [6–9]. Such a boundary condition can further induce longitudinal wrinkles and creases when the sheet is twisted at low tension [10–13] and impact the wavelength of transverse wrinkles at high tension [14,15]. But even before the onset of instabilities, a stretched sheet embodies the complexity of thin sheet elasticity due to geometric nonlinearities even in Hookean (i.e., linear-elastic) materials. This may be one of the reasons why only crude approximations of the prewrinkling state have been considered to address their threshold and morphology [3]. In the following, we focus on the deformation of a longitudinally stretched sheet to highlight the subtle interplay of elasticity and boundary conditions even in the absence of wrinkling.

Equilibrium configurations of an elastic sheet are governed by the biharmonic equation:

$$\Delta^2\phi(x, y) = 0, \tag{1}$$

where $\Delta = (\partial^2/\partial x^2 + \partial^2/\partial y^2)$; x and y are the coordinates along stretching and transverse direction, respectively; and $\phi(x, y)$ is the Airy stress function [16]. Further, $\phi(x, y)$ is defined through $\sigma_{xx} = \partial^2\phi/\partial y^2$, $\sigma_{yy} = \partial^2\phi/\partial x^2$, and $\sigma_{xy} = -\partial^2\phi/\partial x\partial y$, where σ_{ij} with $i, j = x, y$ are the two-dimensional (2D) stress tensor components. The stress σ_{ij} and strain ε_{ij} are linearly related through the standard Hooke's law under plane stress conditions [16]. At the linear order in the displacement, the strain is defined through the displacement field $\mathbf{u} = (u_x, u_y)$ as $\varepsilon_{xx} = \partial u_x/\partial x$, $\varepsilon_{yy} = \partial u_y/\partial y$, and $\varepsilon_{xy} = (\partial u_x/\partial y + \partial u_y/\partial x)/2$. Now, the boundary conditions imposed at an elastic sheet of length L and width W stretched by $\gamma_x = \Delta L/L$ by imposing a relative displacement ΔL between clamped edges reads, along the free edges ($0 < x < L$):

$$\sigma_{yy}(x, 0) = \sigma_{yy}(x, W) = 0, \tag{2}$$

and along the clamped edges ($0 < y < W$):

$$u_x(0, y) = u_y(0, y) = 0, \tag{3}$$

$$u_x(L, y) = \Delta L \text{ and } u_y(L, y) = 0. \tag{4}$$

Harmonic and biharmonic equations with mixed boundary conditions, such as Eqs. (1)–(4), are encountered in various situations in physics including edge effect in electrostatics, wetting phenomena, and crack propagation [17]. In all these examples, the solution is singular as it exhibits a divergence at the location where the boundary condition changes abruptly. In the context of fracture mechanics, it is, for example, crucial to accurately predict the elastic field and the stress concentration developing near the tip of crack. Therefore, powerful methods have been developed to obtain the equilibrium configurations by solving Eq. (1) with appropriate boundary conditions [18–21]. Yet it remains a challenge to obtain analytical expressions over the entire domain. Progress can be made using asymptotic approaches allowing one to obtain the elastic field in a small region surrounding the crack tip. In this intermediate region, it is well known in fracture

mechanics that the elastic field exhibits a self-similar structure characterized by a universal exponent $\alpha = 1/2$ [22].

In a stretched elastic sheet, stress focusing and singularities also occur at the points where clamped edges meet free edges, as first discussed by Williams [23] and then by Bentham [24]. In the case of a semi-infinite long sheet which is clamped at one end, Bentham showed [24] that the longitudinal stress is singular and proportional to $r^{-\alpha}$, where r is the distance from the corner. But, unlike cracks, the exponent of the singularity $0 < \alpha < 1$ depends strongly on the Poisson ratio and geometrical factors. Later, Stern and Soni [25] calculated the displacement fields and stress distribution which is also singular at the corner of a rectangular sheet of semi-infinite extent which is held under mixed free-clamped boundary conditions. As far as we know, these calculated fields have not been tested quantitatively against experiments. Further, because of the difficulty in deriving exact solutions of the equations for elastic sheets, finite-element analysis (FEA) has been increasingly used in structural engineering to obtain stress and strain distributions. The efficacy of those techniques in cases where stress singularities can exist, as at the corners of clamped-free boundary conditions [23] remains unclear. Moreover, the overall shape and displacement field of a finite-sized sheet has not been investigated in any detail.

For materials with large Young's modulus such as steel and glass, the apparent change in shape of a finite-sized sheet is not obvious for typical stresses applied before the material ruptures. In case of softer elastic materials such as latex rubber, the deformation becomes noticeable when examining images in the context of reports on wrinkling in stretched thin sheets [3,6,8]. Because a singularity is present at each of the four corners [24], their interactions can be further important to the observed displacement field of the finite-sized sheet and its edge shape. However, a study of the shape, which can further illuminate the stress distribution in the sheet as it is stretched, has not been reported. This can not only lead to a better understanding of the large deformation regime in elastic materials but also the nature of instability observed in thin sheets under boundary forcing.

In this paper, we discuss experiments on thin elastomer sheets which are clamped at both ends and measurements of their local displacement field with digital image correlation (DIC) technique. Because an analytical expression of the displacement field over the entire sheet is not possible, the experimental results are then compared with numerical simulations using finite-element analysis, assuming a Hookean response of the material. An overall agreement between the experiments and simulations is found. In particular, two regimes of deformations are identified: a uniaxially stretched region in the central part and clamp-dominated regions on the corresponding sides. Within the clamp-dominated region, we find experimentally and numerically that the elastic field is singular near each of the four corners of the sheet. We showed that these results are consistent with the asymptotic analysis of the problem performed by Stern and Soni [25]. Surprisingly, our work is the first experimental validation of their results. Finally, we discuss the regularization of the singularity observed very close to the corners.

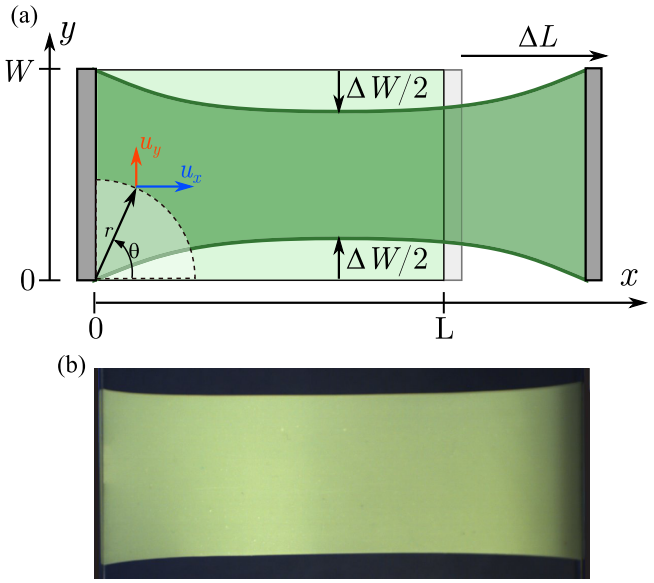

FIG. 1. (a) Schematic of the clamped stretched elastic sheet and the coordinate system. (b) An image of a stretched polyvinyl siloxane sheet ($L = 10$ cm, $L/W = 2$, and $\gamma_x = \Delta L/L = 0.35$).

II. PROTOCOLS

A. Experimental system

In order to investigate the deformation of elastic sheets, we experimentally study elastomers (polyvinyl siloxane and latex rubber) with initial length L, width W, and thickness t. The polyvinyl sheets were fabricated using molds in the laboratory, whereas the latex sheets were bought from a commercial supplier and ironed flat to remove any creases. The sheets were cut to a specified size before being mounted between two parallel flat aluminum clamps as shown schematically in Fig. 1(a). The length and width of the sheet are aligned with the x and y axes of the Cartesian coordinate system with origin corresponding to the bottom left corner of the sheet as shown in Fig. 1(a). The material properties of the sheets, including the Poisson ratio ν and the Young's modulus E, are obtained as part of the analysis of the displacement measurements discussed in the following sections.

The elastic sheet is then stretched by moving one of the clamps which is attached to a motorized linear translating stage. Thus, the clamps stretch the sheet along the x axis, while being held parallel to the y axis. The resulting sheet stretched by a length increment ΔL is also shown schematically in Fig. 1(a), and an actual example corresponding to a polyvinyl sheet is shown in Fig. 1(b). Thus, the current sheet length is $L + \Delta L$ and the corresponding applied strain $\gamma_x = \Delta L/L$. Because of the symmetry of the system, the resulting maximum transverse contraction of the width ΔW can be expected to occur at the middistance between the clamps. Thus, the corresponding width is $W - \Delta W$. We also denote u_x and u_y, the components of the displacement field along the x axis and y axis, respectively, in Fig. 1(a). As shown in Fig. 1(b), we image the sheets against a contrasting background with a digital camera with a resolution of 1824×2048 pixels to obtain the shape of the sheet using white light illumination.

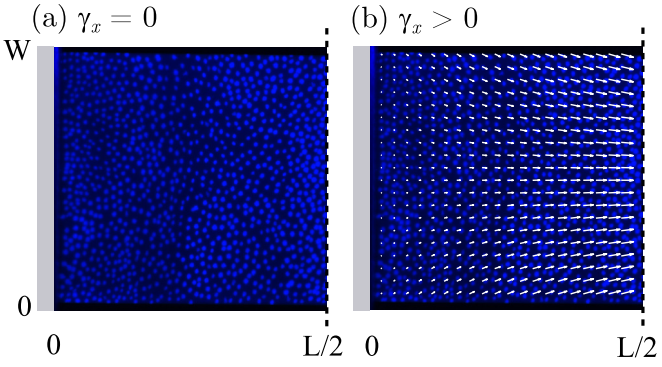

FIG. 2. (a) Image of a sheet with randomly placed markers which fluoresce under UV light with no applied strain $\gamma_x = 0$. (b) Same image with the measured displacement field (white arrows) superimposed under an applied strain $\gamma_x = 0.0375$. Only the left half of the sheet is shown ($L/W = 2, t/W = 1.9 \times 10^{-3}, t = 0.15$ mm).

Thus, we can identify the edge of the sheet by processing the images using standard edge detection algorithms.

B. Displacement field with digital image correlation

The displacement field of the stretched sheet is measured using DIC technique used to measure deformations in elastic medium [26]. This technique requires the surface to have a random texture. Because the surface of the materials used are featureless, we apply markers in a random pattern which fluoresce under UV light as shown in Fig. 2(a). In this technique, the displacement field $\boldsymbol{u}(\boldsymbol{r})$ [with $\boldsymbol{r} = (x, y)$] is related to the intensity fields of the picture by $I_0(\boldsymbol{r}) = I_1(\boldsymbol{r} + \boldsymbol{u})$, where I_0 and I_1 are the intensity fields of the reference image before loading and the image after loading, respectively. The local displacement $\boldsymbol{u}$ of a material point originally at $\boldsymbol{r}$ is obtained by minimizing the cross-correlation function $C(\boldsymbol{u}) = \langle [I_1(\boldsymbol{r} + \boldsymbol{u}) - I_0(\boldsymbol{r})]^2 \rangle$ with respect to $\boldsymbol{u}$ where $\langle ... \rangle$ is an average over a window centered on $\boldsymbol{r}$ with a lateral size which is typically between 8 to 64 pixels, depending on the image resolution. An interpolation of the pictures based on a Fourier decomposition along with a multiscale approach to locate the minimum of C yield a robust and accurate calculation of the displacement with a subpixel resolution [26].

We first consider a latex sheet with size $L = 16$ cm and $W = 8$ cm and thickness $t = 0.15$ mm to investigate the observed displacement field as a function of applied uniaxial strain γ_x. Figure 2(b) shows an example of a displacement field superposed on the reference image when the elastic sheet is stretched by 6 mm ($\gamma_x = 0.0375$). Because of the symmetry of the system, we focus on the left half of the system ($0 < x < L/2$) to not only obtain the data with higher resolution but to show it with higher magnification as well. Here, it is to be noted that only a fourth of the vectors are shown for clarity, i.e., every alternate row and column is skipped to avoid overlaps in the plotting. Because of the size of the cross-correlation window used to detect displacements, the field is effectively averaged over an area of $1.3 \times 1.3\,\text{mm}^2$. This averaging allows for a high precision in the measurement of displacements of the order of 100 μm, corresponding to a resolution of approximately 1×10^{-3} w.r.t. its length, which is of order of the thickness of the sheet. This small averaging window has little impact on the scale of the spatial trends of interest except at the very corners of the sheet.

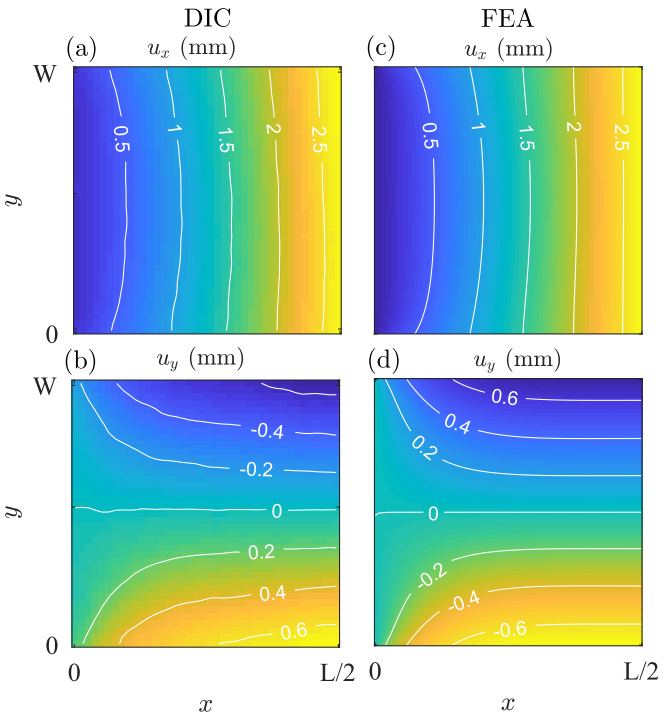

FIG. 3. Maps of the measured u_x (a) and u_y (b) in experiments corresponding to the displacement field shown in Fig. 2(b). The iso-u_x and iso-u_y are also shown. Maps of u_x (c) and u_y (b) obtained with numerical FEA corresponding to the same system as in the experiments along with iso-u_x and iso-u_y contour lines. The experimental and numerical maps are observed to be overall in agreement.

From Fig. 2(b), one observes that the displacement field increases overall in magnitude from the left to the right because the left clamp is fixed and the right clamp (at $x = L$, not shown) is moved. Further, the direction of the arrows indicate that the relative magnitude of the displacement of the sheet in the longitudinal and transverse directions changes continuously with relatively smaller displacements in the transverse direction compared with the longitudinal direction.

To see these trends in the displacement field more quantitatively, the map of u_x is shown in Fig. 3(a) along with iso-u_x contour lines. The complementary map of u_y is shown in Fig. 3(b). We find that the central region of the sheet experiences a uniaxial stretching. Near the clamp, one observes that the sheet displaces not only increasingly with x but also somewhat more greatly at the sides compared with the center axis $y = W/2$ of the sheet. This is apparent from the curvature of the lines denoting the iso-u_y contours in Fig. 3(a) and the iso-u_x contours in Fig. 3(b). Thus, in this region near the clamps, the stretching is biaxial.

C. Finite-element analysis

We perform numerical analysis to further substantiate the experimental measurements. FEA has been used extensively to calculate the displacement fields and stress distributions

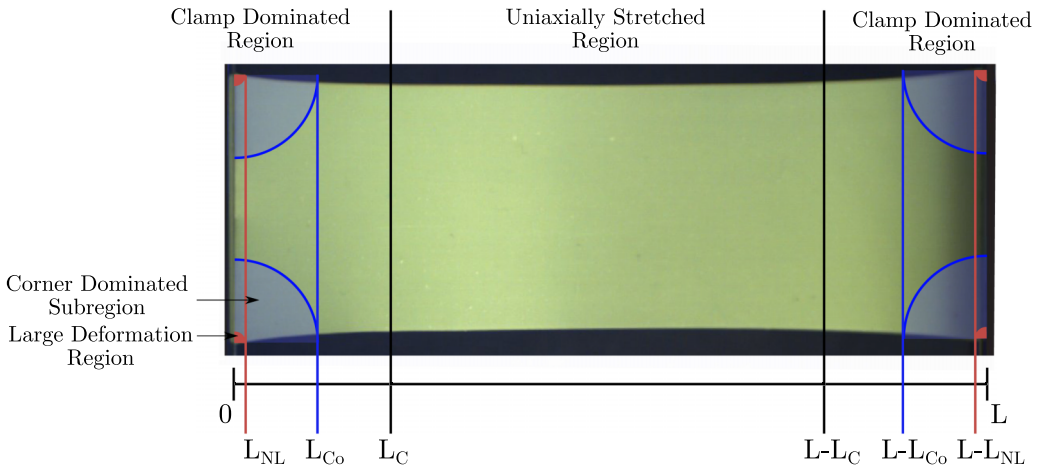

FIG. 4. A symmetric stretched sheet can be divided essentially into two main regions from the clamped boundaries. Further, two subregions can be identified as a function of distance r from a corner. The corresponding distances along strain direction L_C, L_{Co}, L_{NL} are denoted. The corner-dominated region corresponds to $L_{NL} < r < L_{Co}$.

in solids. Even though imposed mixed boundary conditions yields an elastic singularity at each corners of the stretched sheet, we find that Eqs. (1)–(4) solved using the FEA module in MATLAB converges and yields stable results.

The corresponding u_x and u_y maps are shown in Figs. 3(c) and 3(d), respectively, and are observed to be similar to those corresponding to the experiments. In particular, the FEA displacement maps confirms the presence of a uniaxially stretched region and a clamp-dominated region in the stretched elastic sheet with mixed clamped and free boundary conditions at opposite ends.

In the following sections, we will compare the obtained fields using the experimental and numerical methods quantitatively, besides analyzing the observations with asymptotic analysis.

III. DEFORMATION REGIONS IN THE STRETCHED SHEET

From a visual inspection of the displacement field obtained by DIC and, further confirmed by FEA, we identify two regions: (a) a uniaxially stretched region and (b) a clamp-dominated region where the stretch is biaxial as illustrated in Fig. 4. The transition between these two regimes occurs at characteristic distance L_C from the clamps. The clamp length L_C may be expected to be dependent on the Poisson ratio, the sheet geometry, and the applied strain.

As one attempts to understand the deformation of the sheet closer to where the free and clamped edges meet at the four corners in the region $x < L_C$, the displacement field may be characterized by universal features akin to singular field at the vicinity of a crack in a brittle material. Thus, we anticipate the existence of two other characteristics length scales, the corner length $L_{Co}(< L_C)$ and the nonlinear zone length $L_{NL}(< L_{Co})$ near each corner, as illustrated in Fig. 4. For $r > L_{Co}$, the distance from the corner is too large for corner singularity to play a significant role. For $r < L_{NL}$, very close to the corner singularity, we expect that linear elasticity breaks down as is commonly observed in the process zone at the tip of a crack [20]. As a consequence, one may postulate that universal features emerging from the stress singularity may develop over a distance $L_{NL} < r < L_{Co}$.

A. Uniaxially stretched region

We now characterize the linear mechanical properties of the sheet from the DIC measurements in the uniaxially stretched region, i.e., $L_C < x < L - L_C$. We integrate the transverse and longitudinal strains, $\varepsilon_{yy} = -\nu\varepsilon_{xx}$ and $\varepsilon_{xx} = \gamma_x$, respectively, in this region and obtain the displacement fields:

$$u_x = u_0 + \gamma_x x, \tag{5}$$

$$u_y = -\nu\gamma_x(y - W/2), \tag{6}$$

where u_0 is a constant of integration which is dependent on the Poisson ratio and vanishes when $\nu = 0$. From Eqs. (5) and (6), we can readily check that the iso-u_y and iso-u_x are parallel and perpendicular to the longitudinal edges, respectively, which is consistent with the contours shown in Fig. 3. In principle, u_0 is set by matching the solutions at the transition between the uniaxial and biaxial stretching regions. However, it is *a priori* unclear how to perform this in practice.

In Fig. 5(a), we plot the longitudinal displacement profile u_x along the x axis at $y = W/2$. A change of slope is observed near the clamp, signaling the transition to biaxial strain. We then obtain the longitudinal strain measured as the slope of a linear fit of the data in the region where deformations are uniaxial. Using Eq. (5), we find $u_0 = 0.25$ mm, which is much smaller than the sheet length and, thus, it can be neglected to evaluate the local strain, $\varepsilon_{xx} \approx \gamma_x$. In Fig. 5(b), we show the u_y profile along the y axis in the linearly stretched region. The displacements profile decreases linearly with y with no observable effect at the boundaries. From the various applied strain γ_x, we measure the Poisson ratio from the relation $\nu = -\varepsilon_{yy}/\varepsilon_{xx}$ and find $\nu = 0.45 \pm 0.02$ [see Fig. 5(c)].

Finally, we measure the force F for various applied strain. In Fig. 5(d), a plot of the nominal stress $F/(Wt)$ as a function of the applied strain γ_x reveals that the material is linear elastic for $\gamma_x < 0.2$. For larger γ_x, strain softening develops

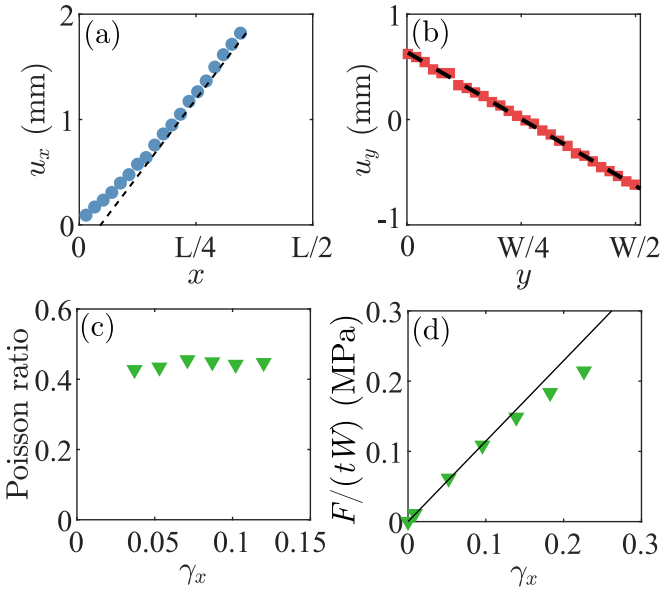

FIG. 5. (a) Displacement profile u_x measured along the x axis at $y = W/2$ for a latex sheet ($L/W = 2$, $t/W = 1.9 \times 10^{-3}$, $t = 0.15$ mm). The clamp induces a slight deviation from linearity near $x = 0$. A linear fit of the data away from the clamp gives $\varepsilon_{xx} = 0.0351$ and $u_0 = 0.25$ mm [see Eq. (5)]. (b) Displacement profile u_y measured along the transverse direction at $x = 3L/4$ in the uniaxially stretched region. A linear fit of the data gives $\varepsilon_{yy} = -0.0159$. (c) The Poisson ratio $\nu = -\varepsilon_{yy}/\varepsilon_{xx}$ is essentially independent of the applied strain γ_x. (d) The nominal stress increases linearly with the strain for $\gamma_x < 0.2$. A linear fit gives $E = 1.1$ MPa.

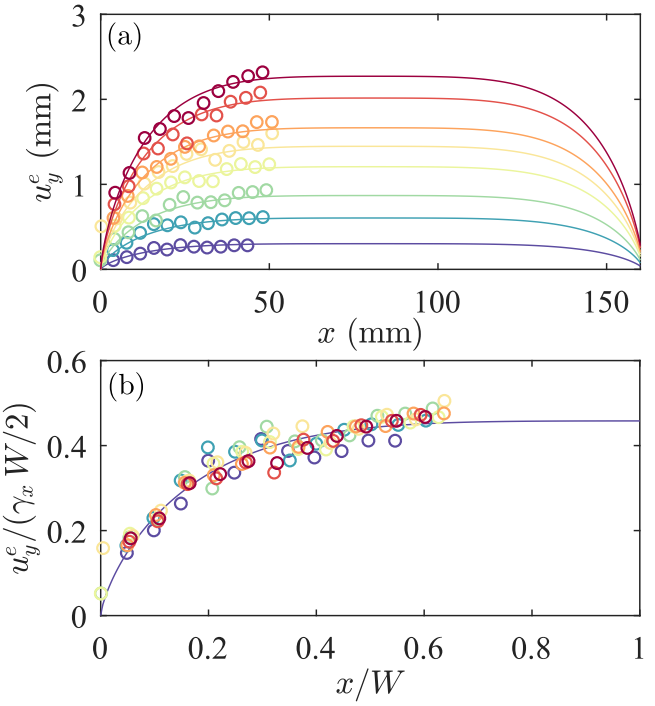

FIG. 6. (a) Measured transverse displacement u_y normalized by $\gamma_x W/2$ for a latex sheet as a function of the normalized longitudinal coordinate x/L for applied strain γ_x in the range 0.09 to 0.30 ($L/W = 2, t/W = 1.9 \times 10^{-3}, t = 0.15$ mm). (b) The data collapse onto a master curve independent of γ_x. The dashed line corresponds to the profile obtained by FEA with $\nu = 0.45$.

as commonly observed in rubbers and elastomers [1]. In this regime, Young's modulus is $E = 1.1$ MPa and the shear modulus defined as $\mu = E/(2(\nu + 1)) = 0.38$ MPa. No hysteresis or permanent deformation were observed on unloading the sample for this entire range even in the nonlinear regime.

B. Edge profile and clamp length scale

We start by analyzing the edge profile u_y^e of the sheet as a function of the applied strain and the aspect ratio L/W. This edge profile simply corresponds to the displacement field of the points at the free edge of the sheet, thus, $u_y^e(x) \equiv u_y(x, 0)$, by definition. In Fig. 6(a), we show the edge profiles measured by DIC for γ_x in the range 0.09−0.30. The aspect ratio of the sheet is $L/W = 2$. At a fixed γ_x, the amplitude of the profile is increasing with x until reaching a stationary value, which indicates that the edges are parallel to the direction of stretch. This is consistent with the fact that the sheet is uniaxially stretched in that region. Thus, using Eq. (6), we have, at $y = 0$, $u_y^e = \nu\gamma_x W/2$, which explains the overall increase of the profile amplitudes with γ_x. Superposing experimental and numerical profiles obtained by FEA (solid lines) for the same γ_x, we observe good agreement, thus validating both the experimental measurements and numerical simulations.

Further, as shown in Fig. 6(b), when normalizing the displacement by $\gamma_x W/2$, we observe a good collapse of the profiles on a master curve not only in the central region but also near the clamps over the entire range of applied strain. Thus, material nonlinearities can be neglected in the range of strain applied.

Next, we explore the role played by the aspect ratio at a fixed applied strain. Experimental data for two different aspect ratios are shown in Figs. 7(a) and 7(b). We observe a good agreement with the numerical profiles calculated by FEA (solid lines). In Fig. 7(c), we plot the normalized profile for aspect ratio in the range 0.5–10 obtained using FEA. For aspect ratios $L/W < 1$, the profiles do not reach a stationary regime, which indicates that, near the free edges, the stretching is biaxial. As the aspect ratio is progressively increased, we observe the development of a flat central region when $W/L > 1$. Interestingly, the normalized profile reaches a maximum larger than ν, which is the maximum value expected from Eq. (6) as highlighted by the arrows in Fig. 7(c). For $L/W \leqslant 2$, we find a unique, global maximum located at the center of the sheet ($x/L = 1/2$). But for $L/W > 2$, we observe the formation of two local maxima near the two opposite clamps (only the left half of the sheet is shown for clarity). These qualitative features could not be observed in the experiments because of material and measurement uncertainties.

To estimate the clamp length experimentally, L_C is defined as the distance from the clamp where $u_y^e(L_C) = \nu\gamma_x W/2$ [a vertical dashed line is shown for the case of $L/W = 10$ in Fig. 7(c)]. This criterion corresponds to the point from where the free edges are essentially parallel. In Fig. 7(d), we plot the measured L_C as a function of the aspect ratio and find that for $L/W > 1$, the clamp length normalized by the width

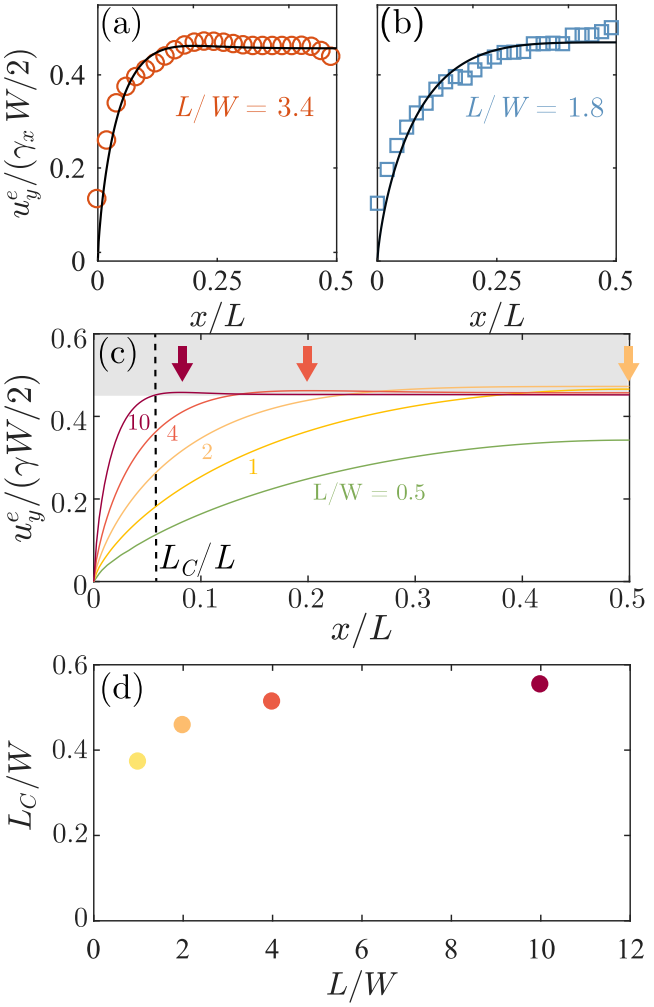

FIG. 7. The observed edge profiles for polyvinyl sheets with two different aspect ratios: (a) $L/W = 1.8$, $W = 6.3\,\text{cm}$, $t = 0.3\,\text{mm}$, and $\gamma_x = 0.25$ and (b) $L/W = 3.3$, $W = 3.1\,\text{cm}$, $t = 0.3\,\text{mm}$, and $\gamma_x = 0.30$. (c) Corresponding profiles obtained with FEA for various L/W indicated are observed to show the same trends observed in the experiments. The arrows indicate the location of the shallow maximum in u_y^e. (d) The estimated L_c increases with L/W to approximately $0.5W \pm 0.05W$.

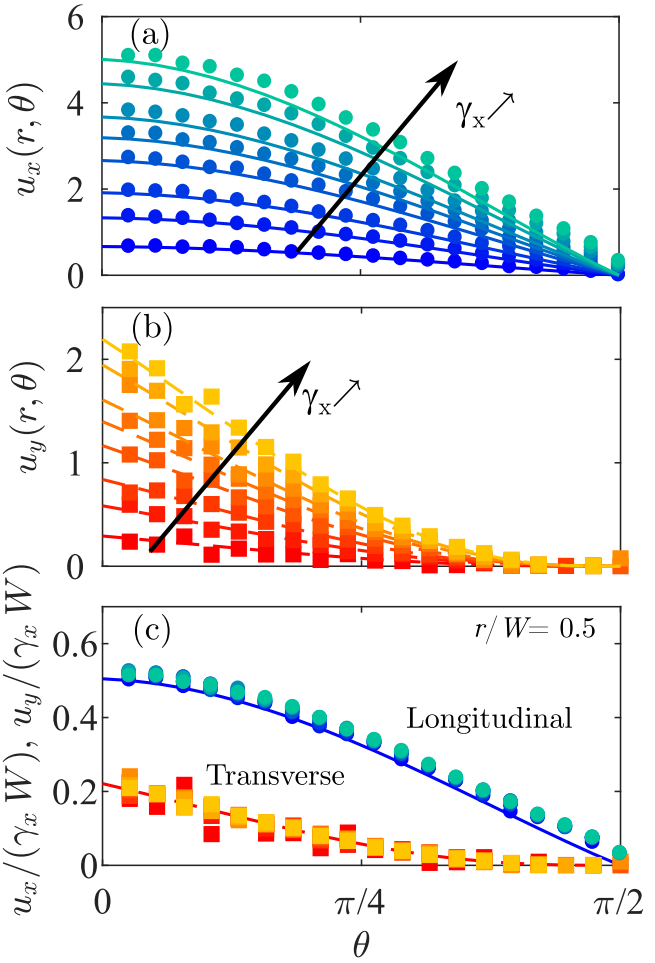

FIG. 8. Longitudinal (a) and transverse (b) displacements profiles as a function of the angle varying γ_x at a fixed distance from the corner $r/W = 0.5$. Solid lines are profiles obtained by FEA. (c) All the profiles collapse on two master curves in excellent agreement with numeric profiles obtained by FEA (solid lines).

is independent of L/W, and $L_C/W = 0.5 \pm 0.2$, where the variation occurs due to the method used to measure L_C.

C. Displacement field in the clamp-dominated region

We now analyze the displacement field inside the sheet. It is convenient to use polar coordinates to express u_x and u_y [see Fig. 1(a) for the notations]. In Figs. 8(a) and 8(b), we plot the longitudinal and transverse displacement profiles obtained by DIC for $r/W = 0.5$ as a function of polar angle θ. The different curves correspond to a fixed strain varied in the range 0.09–0.3. We observe that the overall profiles increase in amplitude with γ_x and that they are smooth functions of θ monotonically decreasing to zero at $\theta = \pi/2$, thus satisfying the imposed boundary conditions at $x = 0$. Excellent collapse of the profiles is obtained when normalizing the displacement by $\gamma_x W$ as shown in Fig. 8(c). Comparing the measured profiles shown in Figs. 8(a)–8(c) with numeric profiles obtained by FEA (solid lines), we obtain a quantitative agreement.

In Figs. 9(a) and 9(b), we analyze the evolution of the displacement profiles with increasing distance from the corner, while keeping the applied strain fixed ($\gamma_x = 0.079$). We obtain a quantitative agreement between the profiles obtained using DIC and FEA, except very close to the corners corresponding to small r/W. At these small distances, we find that the numerical data systematically underestimate the experimental data, although the trend still remain consistent. For the longitudinal displacement, the evolution of the overall amplitude is observed to increase monotonically with r. However, the transverse profiles shown in Fig. 9(b) reveal a more complex dependence with r as the profiles intersect. For example, the profile measured at the largest distance ($r/W = 0.50$) exhibits the largest transverse displacement at $\theta = 0$ but the smallest at around $\theta = \pi/2$. This precludes a successful collapse of the data after a proper rescaling of the displacement, at least in the relatively large range of r considered. Thus, we consider a smaller subregion around the corners to develop further

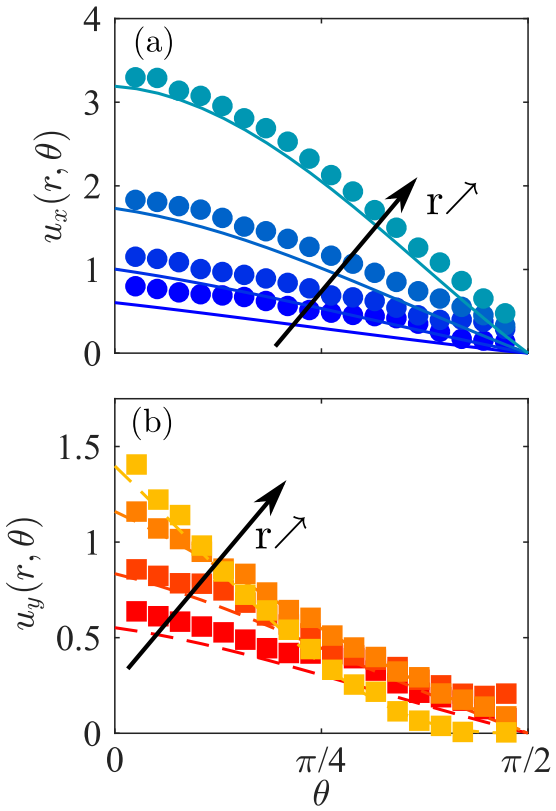

FIG. 9. Longitudinal (a) and transverse (b) displacements profiles as a function of the angle varying the distance from the corner $r/W = 0.063,\ 0.13,\ 0.25$, and 0.50 at fixed $\gamma_x = 0.079$. Solid lines are profiles obtained by FEA.

understanding of the observed displacement field near the clamps in the next section.

IV. CORNER DOMINATED SUBREGION

We start by presenting the analytical results obtained by England [27] and later by Stern and Soni [25] using an asymptotic approach applied near the vicinity of the corner between semi-infinite clamped and free edges.

A. Asymptotic analysis

The displacement components u_x and u_y near a corner upon loading can be decomposed as [25]

$$u_x(r,\theta) = u_x^e(r)\,\Phi_x(\theta)[1+\mathcal{F}(r,\theta)], \tag{7}$$

$$u_y(r,\theta) = u_y^e(r)\,\Phi_y(\theta)[1+\mathcal{H}(r,\theta)], \tag{8}$$

where u_x^e and u_y^e are the longitudinal and transverse displacement at the edge and Φ_x and Φ_y are smooth harmonic functions of θ which depend on ν. We explicitly include higher-order contributions to the displacement field, $\mathcal{F}(r,\theta)$ and $\mathcal{H}(r,\theta)$. These functions encapsulate the complex dependence of the displacement field with r and are responsible for the absence of simple scaling law for u_x and u_y for arbitrary r as evident in Fig. 9(b). However, in the asymptotic limit $r/W \ll 1$, $\mathcal{F}(r,\theta)$ and $\mathcal{H}(r,\theta)$ vanish, yielding a separable form for $u_x(r,\theta)$ and $u_y(r,\theta)$. In this limit, u_x^e and u_y^e read [25]:

$$u_x^e(r) = \frac{g_x(\nu)}{2\mu} K_{\mathrm{I}} r^{\alpha}, \tag{9}$$

$$u_y^e(r) = \frac{g_y(\nu)}{2\mu} K_{\mathrm{I}} r^{\alpha}, \tag{10}$$

where K_{I} is the stress intensity factor in mode I (traction mode), $g_x(\nu)$ and $g_y(\nu)$ are smooth functions of ν, and $\mu = E/[2(1+\nu)]$ is the shear modulus. Further, $\Phi_x(\theta)$ and $\Phi_y(\theta)$ are monotonically decreasing functions with $\Phi_x(0) = \Phi_y(0) = 1$ and $\Phi_x(\pi/2) = \Phi_y(\pi/2) = 0$. The expression for $g_x(\nu)$, $g_y(\nu)$, $\Phi_x(\theta)$, and $\Phi_y(\theta)$ can be found in Appendix. The exponent α is the solution of [25]:

$$\cos\alpha = \frac{2\alpha^2}{\kappa} - \frac{\kappa^2+1}{2\kappa}, \tag{11}$$

where $\kappa = (3-\nu)/(1+\nu)$ in case of plane stress. For an incompressible material $\nu = 0.5$, and thus $\kappa = 5/3$, $\alpha = 0.69 \approx 2/3$, and $\mu = E/3$. In the case of the materials used in our experiments where $\nu = 0.45$, we have $\alpha = 0.71$. Because the amplitude of the displacement grows sublinearly with r, the stress is singular at the four corners. Indeed, we have $\sigma_{rr} \sim \mu \partial u_r/\partial r$, and thus $\sigma_{rr} \sim K_{\mathrm{I}} r^{\alpha-1}$, with $\alpha < 1$, which diverges as r goes to zero. This is obviously unphysical as was already noted by Williams [23]. Therefore, it is necessary to introduce a cutoff length at a small scale below which the asymptotic solution is no longer valid.

The functional dependence of the stress intensity factor with the applied loading, mechanical properties, and the sheet dimensions has not been yet given. By dimensional analysis, we expect:

$$K_{\mathrm{I}} = k_{\mathrm{I}}(\nu)\frac{F}{A} W^{1-\alpha}, \tag{12}$$

where k_{I} is a smooth function of ν. As the Poisson ratio ν tends to zero, the stress field is uniaxial over the entire length of the sheet, without any biaxial stress building up in the clamp-dominated region. Therefore, we expect that clamp-dominated region to disappear altogether with the elastic singularity. Then, we argue that, as $\nu \to 0$, the extension of the clamp-dominated region L_C scales as $L_C \sim W\nu^{\gamma}$ ($\gamma > 0$), and the strength of the singularity scale $K_{\mathrm{I}} \sim k_{\mathrm{I}} \sim \nu^{\beta}$ ($\beta > 0$).

B. Range of validity of the asymptotic displacement field

As argued earlier, the asymptotic solutions derived within a linear elasticity framework are expected to be accurate over a finite range of distance from the corner, bounded from below by the large deformation or nonlinear zone and from above by the fact that the sheet is finite sized. Therefore, to compare the asymptotic solution with experiments, it is crucial to address its range of validity and evaluate the cutoff lengths at small and larger scales which can depend on the Poisson ratio, sheet geometry, and applied strain.

Now, the higher-order terms in the Eqs. (7) and (8) become of the same order as the singular terms, far enough from the corner. Since analytic expressions for the higher-order terms are not available, we resort to discussing the range of

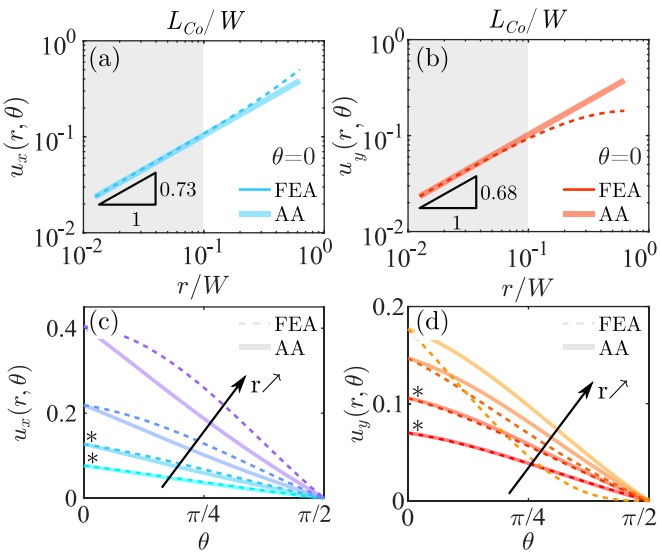

FIG. 10. The dependence of the longitudinal displacement u_x (a) and transverse displacement u_y (b) with distance from the corner r for $\theta = 0$. Good agreement between numerics (dashed lines) and asymptotic analysis (solid lines) is obtained for $r/W < L_{Co}/W = 0.1$. Profiles are obtained by FEA (dashed lines) and asymptotic analysis (solid lines). θ dependence of u_x (c) and u_y (d) for $r/W = 0.063$, 0.1, 0.25, and 0.5. Good agreement between numerics (FEA, dashed lines) and asymptotic analysis (AA, solid lines) is obtained for $r < L_{Co} = 0.1\,W$.

validity of the asymptotic predictions based on the numerical results. The longitudinal and transverse displacements along the direction $\theta = 0$ are shown in a log-log plot in Figs. 10(a) and 10(b), respectively. We define the corner length L_{Co} as the distance below which the numeric profile and asymptotic prediction are in agreement to within 10% relative difference. With this definition, we obtain a measure of the corner length, $L_{Co} = 0.1\,W$. For $r < L_{Co}$, a fit of the data gives $u_x(r,0) \sim r^{0.73}$ and $u_y(r,0) \sim r^{0.68}$, in good agreement with prediction of $\alpha = 0.71$ in case where $\nu = 0.45$ by Stern and Soni [25].

Next we analyze the angular dependence of the displacement field. In Figs. 10(c) and 10(d), we plot the longitudinal and transverse displacement as a function of θ for r/W in the range 0.0625–0.5. Consistent with previous comparisons, we obtain good agreement between numerics (dashed lines) and asymptotic analysis (solid lines) for $r/W < L_{Co}/W = 0.1$, corresponding to the profiles with a star label.

C. Small-scale cutoff

Now we focus on the small-scale cutoff below which the model equations used cannot be expected to be valid. It has been long realized [23] that the divergence of the stress at the singularity is not physical and is regularized by nonlinear processes which operate in any material at sufficiently large stresses. Such processes mean that the linear elastic equations used are no long valid. For example, in fracture mechanics, which is governed by similar elastic equations [19,20,22], a *fracture process zone* is well known to occur near the tip of a fracture due the singular nature of the solutions there. The nature of the nonlinear processes and the size of the process zone are highly dependent on the type of material, the type of loading, and the geometry of the sample. In our experiments, we did not observe irreversible deformation due to plasticity or damage with the material used over the range of applied strain. Thus, nonlinear elastic (reversible) deformations alone may suffice to regularize the singularity at the corner.

Assuming that elastic nonlinearity becomes dominant for stresses $\sigma \sim \mu$ or strain of $\mathcal{O}(1)$, we can provide a natural length scale L_{NL} below which linear elasticity breaks down. From Eqs. (9) and (10), the typical strain experience at a distance r is given by $\varepsilon \sim K_I/\mu r^{\alpha-1}$. Thus, when $r \approx L_{NL}$, $K_I/\mu L_{NL}^{\alpha-1} \sim 1$, yielding $L_{NL} \sim (K_I/\mu)^{1/(\alpha-1)}$. Using Eq. (12), we obtain:

$$L_{NL}/W = f(\nu)\,\gamma_x^{1/(1-\alpha)}, \tag{13}$$

where $f(\nu)$ is an unknown function of ν which should vanish as $\nu \to 0$. Similar scaling for the extent of the process zone, where nonlinearities dominate, has been derived in the context of crack propagation in gels and adhesives [28–30]. With the typical strain and width used in the experiment ($\gamma_x \sim 0.1$, $W = 80$ mm), and assuming that f is $\mathcal{O}(1)$ for incompressible material, $L_{NL}/W \sim 10^{-3}$, and thus L_{NL} is of order 0.1 mm. This length scale is of order of the spatial accuracy of the DIC technique and the thickness of the sheet and cannot be clearly resolved in our experiments. With the geometrical and loading parameters used in the study, Eq. (13) yields a regularized region based on nonlinear elastic effect of order of the thickness. For a thick-enough sheet, 3D elasticity effects may take over near the clamps before the development of large stresses predicted by Stern and Soni. More work is needed to investigate the crossover between 2D and 3D elasticity for very thin sheets, especially the regime where $t \ll L_{NL}$.

D. Comparisons with DIC and FEA methods

We now compare the results obtained from experiments and simulations with the predictions from the asymptotic analysis having obtained the inferred range of $L_{NL} < r < L_{Co}$, where $L_{NL}/W = 10^{-3} \sim 0$ and $L_{Co}/W = 0.10$. In Fig. 11, we show in a log-log plot, the transverse displacement at the edge u_y^e normalized by $\gamma_x W/2$ as a function of x/W (see inset). We find that the experimental profiles are compatible with the theoretical prediction and FEA profiles after introducing a small offset $x_s/W = -0.01$ in the x axis. Because edge profile develops a power-law behavior over a range of length scales which are difficult to reach experimentally, the agreement with theory is very sensitive to an offset in the origin of the x axis.

Next we compare the θ dependence of the experimental displacements field with theoretical predictions for $r/W = 0.0625$, 0.10, 0.2, and 0.25 in Fig. 12. For $r/W < L_{Co}/W = 0.1$, we expect that the experimental profiles measured at various distance from the corner collapse on a single power law when normalized by r^α with $\alpha = 0.71$. In Fig. 12(a), we plot the longitudinal displacement normalized by $\gamma_x W^{1-\alpha} r^\alpha$ ($\sim r^\alpha$) as a function of θ. We observe a good collapse of the data when $\alpha = 0.71$. For comparison, in the inset, we show the effect of a rescaling using $\alpha = 1$. Although the evolution of the profile is consistent with numeric profiles obtained by FEA (dashed line), the experimental profiles are shifted

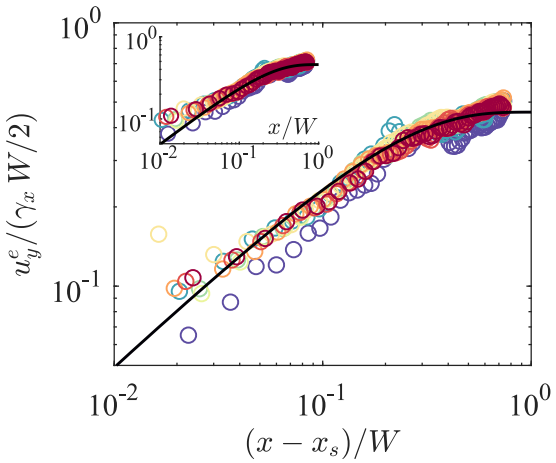

FIG. 11. Normalized edge profile from experiment (colored disks) and numeric simulations (solid line) as a function of x/W. Measured profile exhibits a power law compatible with numeric profiles and theoretical predictions introducing an offset $x_s/W = -0.01$. Insets: Same data without offset.

upward by an overall constant. Then, we show the result of the same analysis for the transverse displacement in Fig. 12(b). We observe a better collapse of the data using $\alpha = 0.71$ than $\alpha = 1$ (see inset), confirming that the displacement field is singular at the corners.

Thus, we clearly find that the strain and stress fields are controlled by a nontrivial exponent. Although the experimental data do not allow a precise measure of the exponent of the singularity, we demonstrate unambiguously that it is smaller than unity, confirming the existence of an elastic singularity at the corners of a longitudinally stretched sheet.

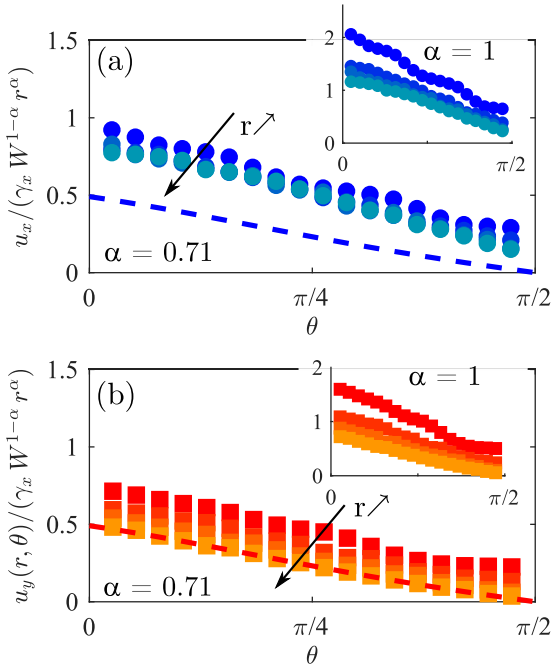

FIG. 12. Displacement profiles in the longitudinal (a) and transverse (b) direction measured at a distance $r = 5$, 10, 15, 20 mm from the corner ($\gamma_x = 0.09$). A good collapse of the data is obtained when the displacements are normalized using $\alpha = 0.71$ rather than $\alpha = 1$ (see inset).

V. CONCLUSIONS

In summary, we obtain the displacement field and the shape of elastic sheets under longitudinal stretching with complementary experimental and theoretical models. In particular, we accurately measure the local displacements experienced by the sheet using DIC techniques over a wide range of applied strains. We also calculate the displacement field using finite-element analysis with equations used to model planar deformation of sheets under boundary applied stresses. This numerical analysis is performed with the same-sized sheets as in the experiments but assuming that the thickness of the sheet does not evolve, even when a significant range of strain is applied. Nonetheless, we find that linear elasticity provides a reasonable description of the overall displacement field and shape of the free edges for applied strained γ_x at least up to 0.3.

While a reasonably simple form of the elastic equations are found to describe the overall deformations, these equations cannot be fully solved analytically. Thus, to make progress toward developing an analytical framework to understand the observed sheet displacement field, we identify regions and subregions in the deformed sheet which are amenable to further analysis. We find that the sheet can be divided overall into a simple uniaxially stretched central region and a more complex clamp-dominated region near each clamped edge. The length scale from the clamps where linear uniaxial stretching occurs can be understood as resulting from a trade-off between satisfying the no-slip boundary condition imposed at the clamps and minimizing the additional elastic energy induced by the transverse stresses.

Further, inside the clamp-dominated regions, we identify two subregions depending on the distance from each clamped-free corner of the sheet. In the corner-dominated subregion, we find that asymptotic analysis, performed in the context of sheets with semi-infinite clamped and free edges under strain by Stern and Soni [25], is found to be in excellent agreement with FEA analysis both for the evolution of the displacement field with distance from the corner ($\sim r^\alpha$ with $\alpha = 0.71$ for Poisson ratio $\nu = 0.45$) and the angular dependence. The extent of this subregion characterized by a diverging stress is found to be of order $L_{\mathrm{Co}} = 0.1\, W$ for the elastomers used. We show that asymptotic and FEA analysis give a reasonable description of the measured displacement fields obtained by DIC technique. While the power law $u_y \sim r^\alpha$ could not be checked experimentally in terms of distance r because of a lack of sufficient range of length scales within the corner-dominated zone, we observe good agreement between the asymptotic solutions and the experiments for the angular dependence. Further, we infer that the derived power law of 0.71 is consistent with our measurements. Very close to the corners, we postulate the existence of a large deformation subregion where nonlinear process may occur because of the large diverging stresses there, analogously to the process zone in fracture mechanics. However, due to the lack of permanent

deformation on stretching, we expect that the corner singularity to be regularized by nonlinear elasticity.

Finally, from the perspective of wrinkling in elastic sheets, we confirm with our experiments that a stretched sheet remains planar because the sheet thickness chosen in our study are above the critical threshold required for wrinkling [6,8]. In the case where transverse wrinkles are observed in sheets with [15] or without twist [6], it was observed that the wrinkles form only in the central regions and are suppressed near the clamped boundaries to a distance which is of order of half the width of the sheet. With our analysis of the clamp length L_C, we provide a quantitative characterization of the range over which the clamps induce a significant contribution to elastic field which has important implications to the development of models of tensional wrinkling. According to our study, the stress fields in the corner-dominated subregion extend from each corner to a similar distance. This biaxial stretching appears to suppress the formation of wrinkles in that region even when the sheet is thin enough to display transverse wrinkles. The observed extent of the corner-dominated subregion may be further consistent with reports [6,8] that wrinkles are not observed for sheets with L/W well below two, even in case of sufficiently thin sheets. Future work is required to connect the comprehensive analysis of the state of stress of the sheet provided by our study in the prewrinkling regime to the occurrence and extent of wrinkling in thin sheets.

ACKNOWLEDGMENT

This work was supported by the National Science Foundation under Grant No. DMR 1508186.

APPENDIX: AUXILIARY FUNCTIONS FOR THE ASYMPTOTIC DISPLACEMENT FIELDS

The analytic expressions of the asymptotic displacement fields we use are adapted from Stern and Soni [25]. There fields were formulated using polar coordinates. Here we provide the corresponding formulations using Cartesian coordinates by introducing auxiliary functions:

$$g_x(\nu) = f_r^{\mathrm{I}}(0) + \eta f_r^{\mathrm{II}}(0), \tag{A1}$$

$$g_y(\nu) = f_\theta^{\mathrm{I}}(0) + \eta f_\theta^{\mathrm{II}}(0), \tag{A2}$$

where $\eta = K_{\mathrm{I}}/K_{\mathrm{II}}$ is the mixed-mode ratio and K_{I} and K_{II} are the equivalent of the stress intensity factors and depend on the applied load and ν. The mixed-mode ratio is given by

$$\eta = \frac{\sin(\alpha\pi)}{\kappa + 2\alpha + \cos(\alpha\pi)}, \tag{A3}$$

where α is the exponent of the singularity which is given by Eq. (11). Equation (A3) implies that the local elastic field near the corner always includes an opening mode and a shear mode as commonly observed in interfacial crack between two different materials [31].

Then the expressions for $\Phi_x(\theta)$ and $\Phi_y(\theta)$ read:

$$\Phi_x(\theta) = g_x^{-1}(\nu)\left[f_r^{\mathrm{I}}(\theta) + \eta\, f_r^{\mathrm{II}}(\theta)\right]\cos\theta, \tag{A4}$$

$$- g_x^{-1}(\nu)\left[f_\theta^{\mathrm{I}}(\theta) + \eta\, f_\theta^{\mathrm{II}}(\theta)\right]\sin\theta, \tag{A5}$$

$$\Phi_y(\theta) = g_y^{-1}(\nu)\left[f_r^{\mathrm{I}}(\theta) + \eta\, f_r^{\mathrm{II}}(\theta)\right]\sin\theta, \tag{A6}$$

$$+ g_y^{-1}(\nu)\left[f_\theta^{\mathrm{I}}(\theta) + \eta\, f_\theta^{\mathrm{II}}(\theta)\right]\cos\theta, \tag{A7}$$

where

$$f_r^{\mathrm{I}}(\theta) = (\kappa-\alpha)\cos[(1-\alpha)(\pi/2-\theta)] - (\kappa-a)\cos[(1+\alpha)(\pi/2-\theta)], \tag{A8}$$

$$f_r^{\mathrm{II}}(\theta) = -(\kappa-\alpha)\sin[(1-\alpha)(\pi/2-\theta)] + (\kappa+a)\sin[(1+\alpha)(\pi/2-\theta)], \tag{A9}$$

$$f_\theta^{\mathrm{I}}(\theta) = (\kappa+\alpha)\sin[(1-\alpha)(\pi/2-\theta)] - (\kappa-a)\sin[(1+\alpha)(\pi/2-\theta)], \tag{A10}$$

$$f_\theta^{\mathrm{II}}(\theta) = (\kappa+\alpha)\cos[(1-\alpha)(\pi/2-\theta)] - (\kappa+\alpha)\cos[(1+\alpha)(\pi/2-\theta)]. \tag{A11}$$

[1] R. S. Rivlin and D. Saunders, Philos. Trans. R. Soc. Lond. A **243**, 251 (1951).

[2] L. R. G. Treloar, *The Physics of Rubber Elasticity* (Oxford University Press, Oxford, UK, 1975).

[3] E. Cerda and L. Mahadevan, Phys. Rev. Lett. **90**, 074302 (2003).

[4] J. S. Huang, B. Davidovitch, C. D. Santangelo, T. P. Russell, and N. Menon, Phys. Rev. Lett. **105**, 038302 (2010).

[5] N. Friedl, F. Rammerstorfer, and F. Fischer, Comput. Struct. **78**, 185 (2000).

[6] V. Nayyar, K. Ravi-Chandar, and R. Huang, Int. J. Solids Struct. **48**, 3471 (2011).

[7] T. Y. Kim, E. Puntel, and E. Fried, Int. J. Solids Struct. **49**, 771 (2012).

[8] T. J. Healey, Q. D. Li, and R. B. Cheng, J. Nonlinear Sci. **23**, 777 (2013).

[9] M. Taylor, K. Bertoldi, and D. J. Steigmann, J. Mech. Phys. Solids **62**, 163 (2014).

[10] A. E. Green, Proc. R. Soc. A **161**, 197 (1937).

[11] J. Chopin and A. Kudrolli, Phys. Rev. Lett. **111**, 174302 (2013).

[12] A. P. Korte, E. L. Starostin, and G. H. M. van der Heijden, Proc. R. Soc. A **467**, 285 (2011).

[13] J. Chopin and A. Kudrolli, Soft Matter **12**, 4457 (2016).

[14] J. Chopin, V. Demery, and B. Davidovitch, J. Elast. **119**, 137 (2015).

[15] A. Kudrolli and J. Chopin, Proc. R. Soc. A **474**, 20180062 (2018).

[16] L. D. Landau and E. Lifshitz, Course Theor. Phys. **3**, 109 (1986).

[17] J. Eggers and M. A. Fontelos, *Singularities: Formation, Structure, and Propagation* (Cambridge University Press, Cambridge, 2015), Vol. 53.

[18] N. I. Muskhelishvili, *Some Basic Problems of the Mathematical Theory of Elasticity* (Springer Science & Business Media, Berlin, 2013).
[19] J. B. Leblond, *Mécanique de la Rupture Fragile et Ductile* (Hermes Science Publications, Paris, 2003).
[20] K. B. Broberg, *Cracks and Fracture* (Elsevier, Amsterdam, 1999).
[21] G. C. Sih, *Methods of Analysis and Solutions of Crack Problems*, (Springer Science & Business Media, Berlin, 2013), Vol. 1.
[22] C.-T. Sun and Z. Jin, *Fracture Mechanics* (Elsevier, Oxford, 2012).
[23] M. Williams, J. Appl. Mech. **19**, 526 (1952).
[24] J. Benthem, Q. J. Mech. Appl. Math. **16**, 413 (1963).
[25] M. Stern and M. L. Soni, Int. J. Solids Struct. **12**, 331 (1976).
[26] F. Hild and S. Roux, Strain **42**, 69 (2006).
[27] A. England, Int. J. Eng. Sci. **9**, 571 (1971).
[28] T. Baumberger, C. Caroli, D. Martina, and O. Ronsin, Phys. Rev. Lett. **100**, 178303 (2008).
[29] E. Bouchbinder, T. Goldman, and J. Fineberg, Rep. Prog. Phys. **77**, 046501 (2014).
[30] C. Creton and M. Ciccotti, Rep. Prog. Phys. **79**, 046601 (2016).
[31] J. Hutchinson and Z. Suo, Adv. Appl. Mech. **29**, 63 (1992).